Chapter 4: Observations: Changes in Snow, Ice and Frozen Ground
Figures

Coordinating Lead Authors: Peter Lemke (Germany), Jiawen Ren (China)

Lead Authors: Richard Alley (USA), Ian Allison (Australia), Jorge Carrasco (Chile), Gregory Flato (Canada), Yoshiyuki Fujii (Japan), Georg Kaser (Austria), Philip Mote (USA), Robert Thomas (USA), Tingjun Zhang (USA)

Contributing Authors: Jason Box (USA), David Bromwich (USA), Ross Brown (Canada), Graham Cogley (Canada), Joey Comiso (USA), Mark Dyurgerov (USA), Blair Fitzharris (New Zealand), Oliver Frauenfeld (USA), Helen Fricker (USA)**,** Hilmar Gudmundsson (UK), Christian Haas (Germany), Jon Ove Hagen (Norway), Charles Harris (UK), Larry Hinzman (USA), Regine Hock (Sweden), Martin Hoelzle (Switzerland), Philippe Huybrechts (Belgium), Ketil Isaksen (Norway), Peter Jansson (Sweden), Adrian Jenkins (UK), Ian Joughin (USA), Christoph Kottmeier (Germany), Ron Kwok (USA), Seymour Laxon (UK), Shiyin Liu (China), Douglas MacAyeal (USA), Humphrey Melling (Canada), Atsumu Ohmura (Switzerland), Anthony Payne (UK), Terry Prowse (Canada), Bruce Raup (USA), Charlie Raymond (USA), Eric Rignot (USA), Ignatius Rigor (USA), David Robinson (USA), Drew Rothrock (USA), Simon Scherrer (Switzerland), Sharon Smith (Canada), Olga Solomina (Russia), David Vaughan (UK), John Walsh (USA), Anthony Worby (Australia), Tomomi Yamada (Japan), Lin Zhao (China)

Review Editors: Roger Barry (USA), Toshio Koike (Japan)

Date of Draft: 27 October 2006

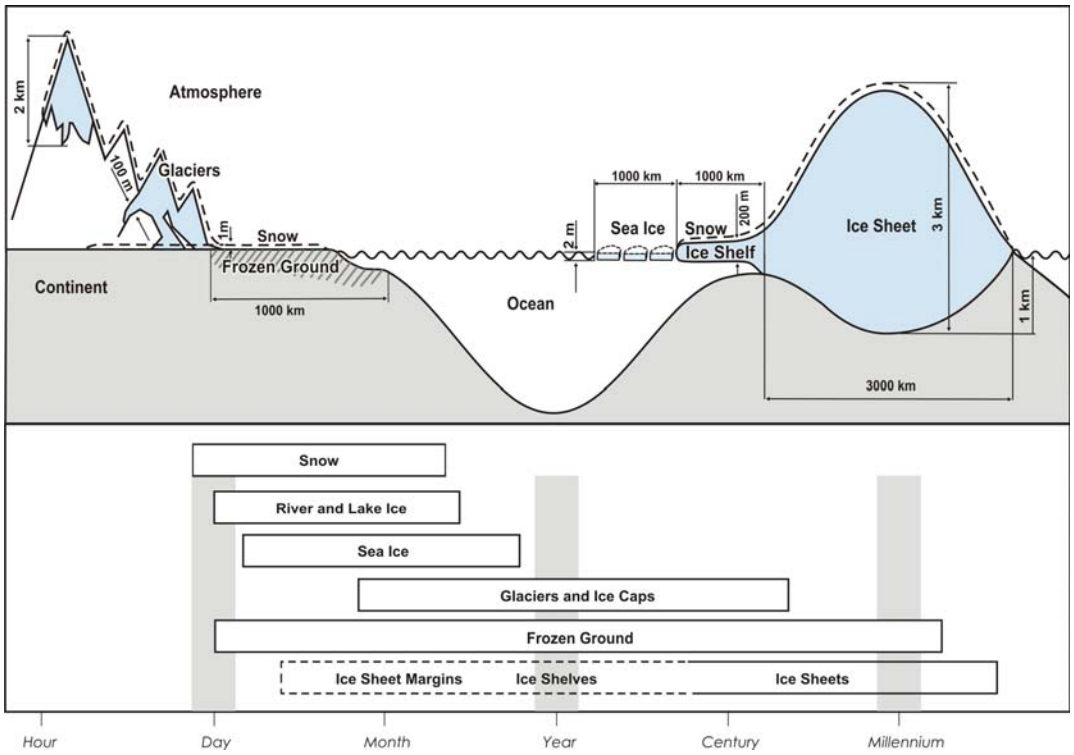

Figure 4.1. Components of the cryosphere and their time-scales.

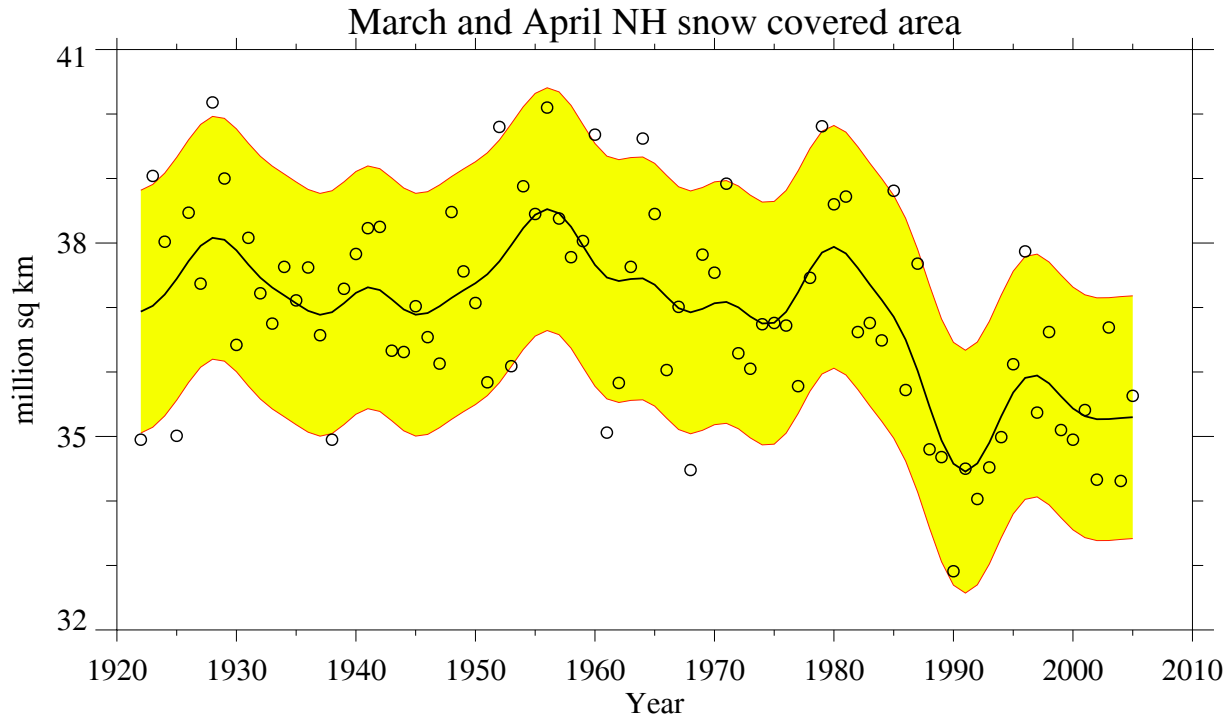

Figure 4.2. Update of NH March-April snow covered area (SCA) from Brown (2000). Values of SCA before 1972 are based on the station-derived snow cover index of Brown (2000); values beginning in 1972 are from the NOAA satellite dataset. The smooth curve is derived using the same 13-point filter as in Chapter 3, and the shaded area shows the 5–95% range of the data estimated after first subtracting the smooth curve.

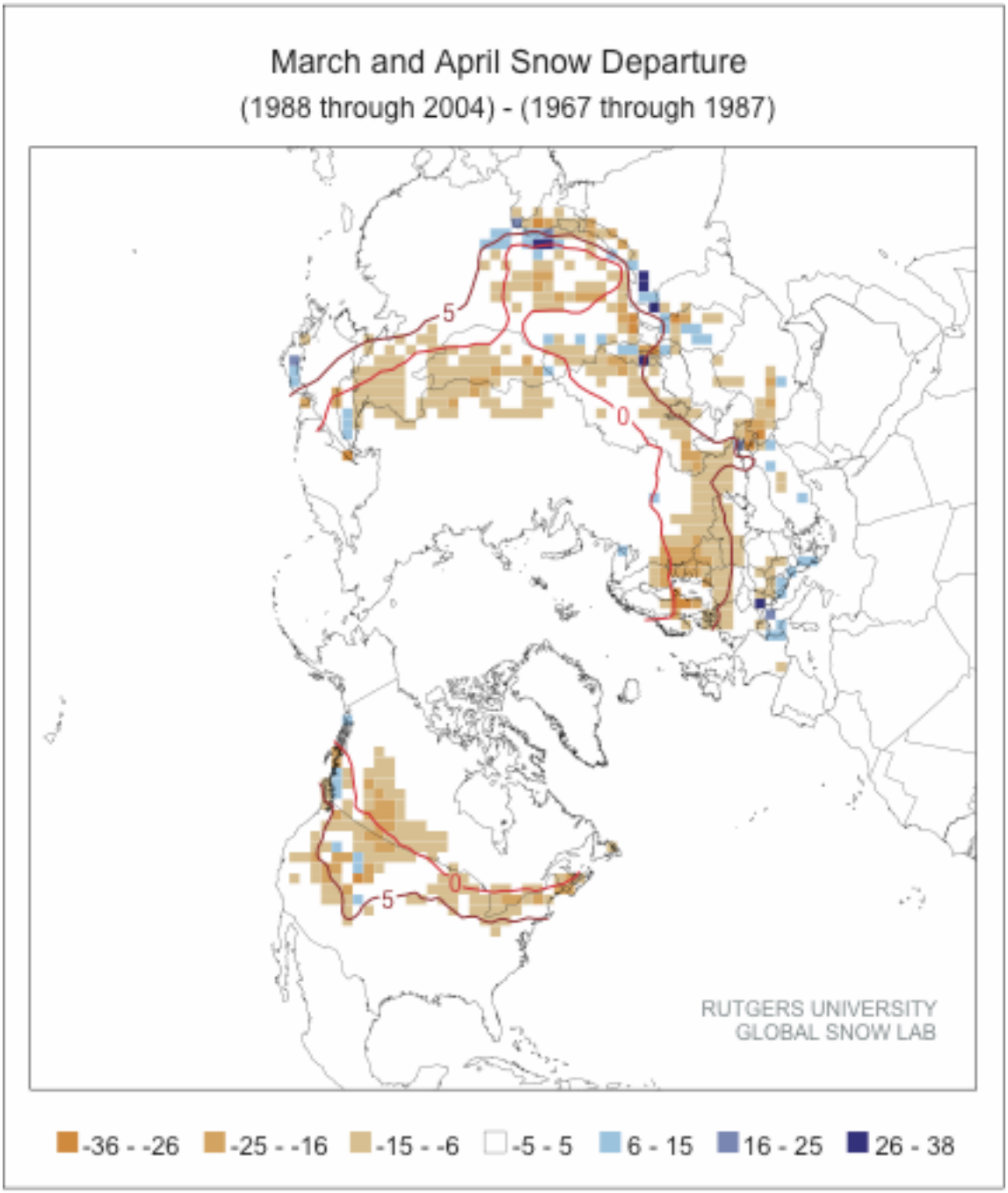

Figure 4.3. Differences in the distribution of Northern Hemisphere March-April snow cover between earlier (1967–1987) and later (1988–2004) portions of the satellite era (expressed in percent coverage). Negative values indicate greater extent in the earlier portion of the record. Extents are derived from NOAA/NESDIS snow maps. Red curves show the 0°C and 5°C isotherms averaged for March and April 1967–2004, from the CRUTEM2v data (www.cru.uea.ac.uk).

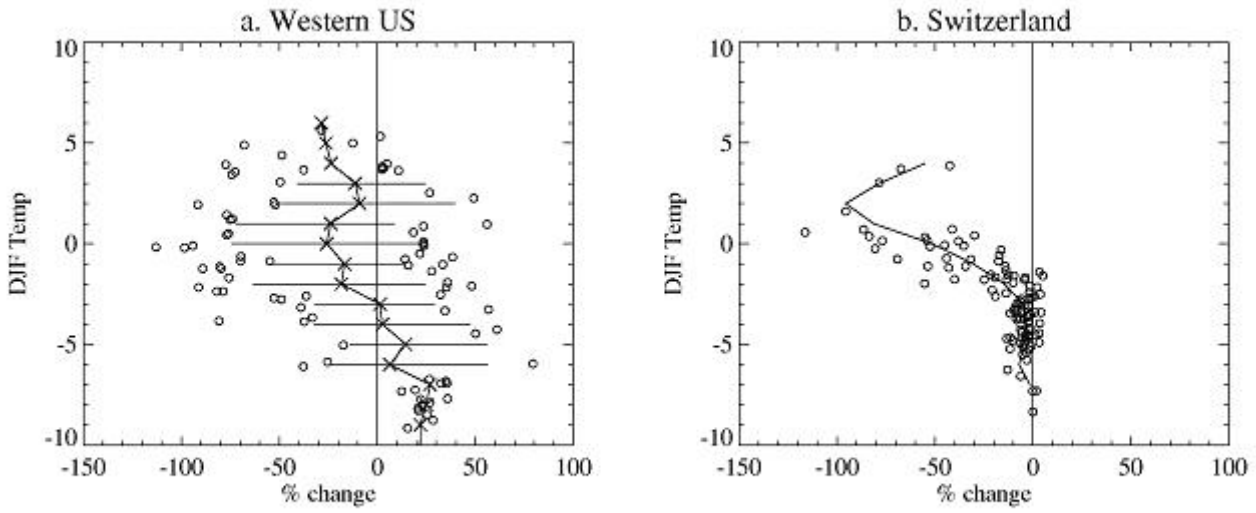

Figure 4.4. Dependence of trends in snow on mean winter temperature (°C) at each location. (a) Relative trends in 1 April snow water equivalent, 1950–2000, in the mountains of western North America (British Columbia, Washington, Oregon, and California), binned by mean December–February (DJF) temperature. For each 1°C temperature bin, '×' symbols indicate the mean trend, bars indicate the span from the 5% to the 95% range for bins with at least 10 points, and circles indicate outliers. Total number of data points is 323. Adapted from Mote et al. (2005). (b) Relative trend in days of winter (December-February) snow cover at 109 sites in Switzerland, 1958–1999, binned by mean DJF temperature. Adapted from Scherrer et al., 2004.

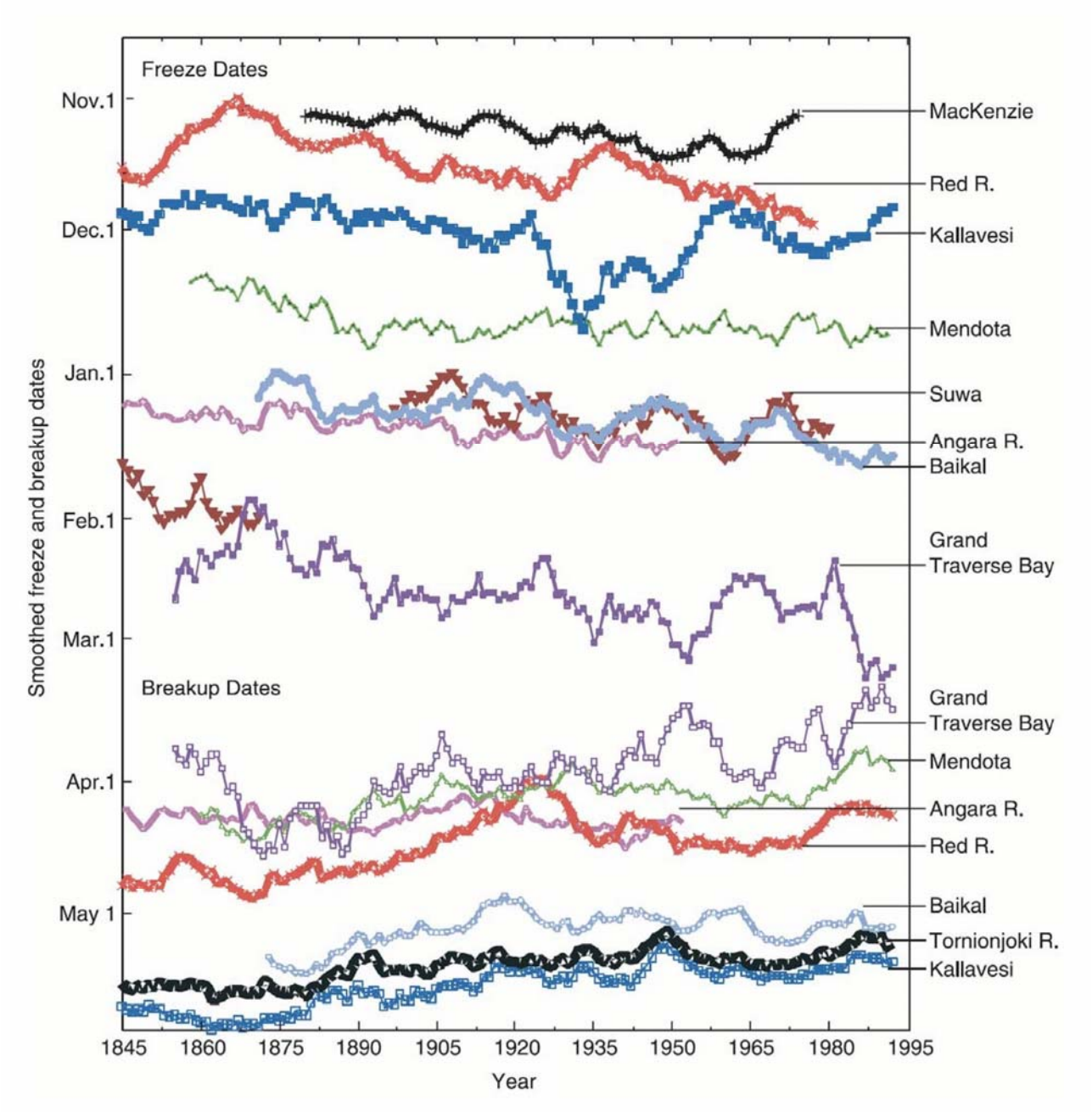

Figure 4.5. Time series of freeze-up and break-up dates from several northern lakes and rivers (Reprinted with permission from Magnuson et al., 2000, Copyright AAAS). Dates have been smoothed with a 10-year moving average. See the cited publication for locations and other details.

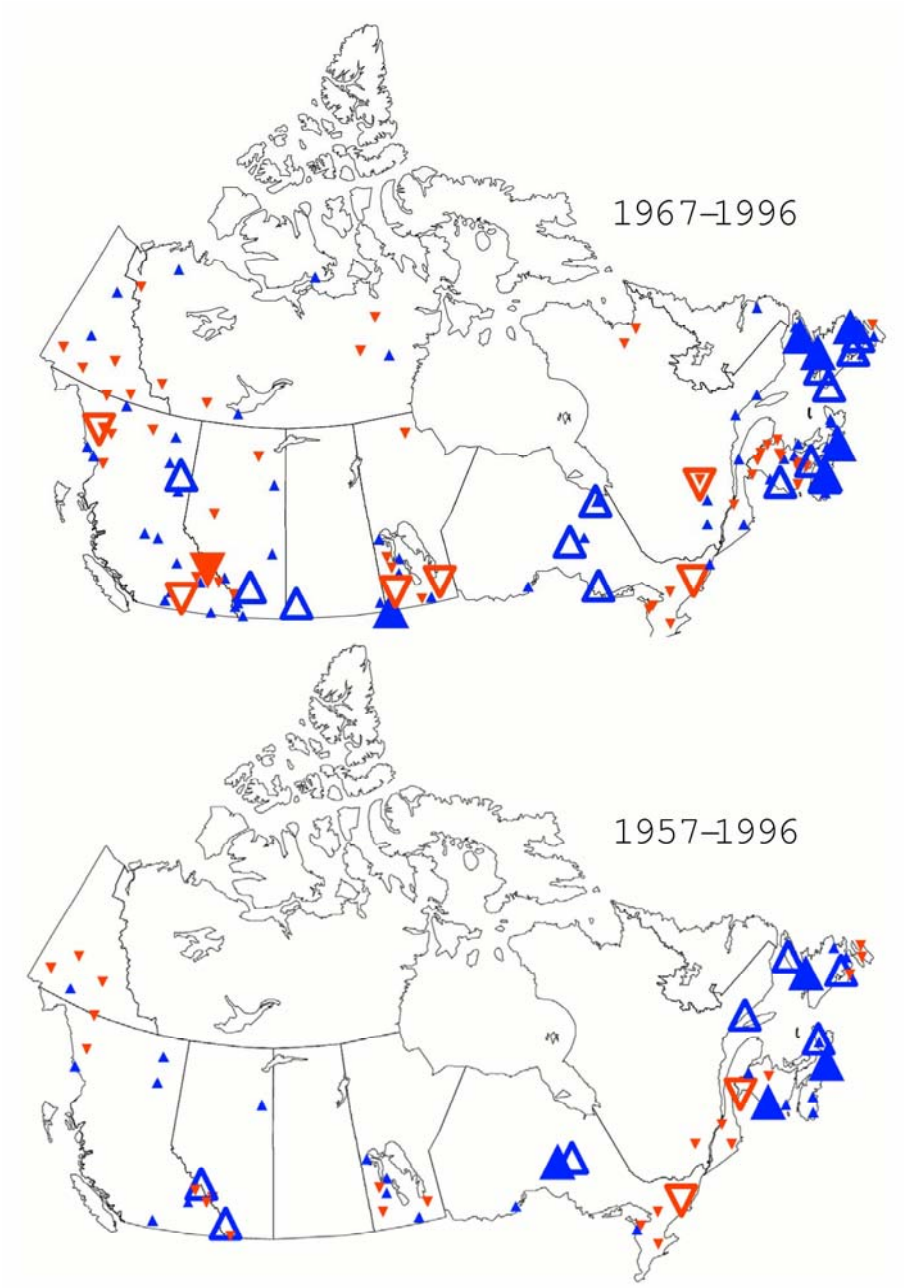

Figure 4.6. Trends in river ice-cover duration in Canada. Upward pointing triangles indicate lengthening of the ice-cover period while downward triangles indicate shortening of the ice-cover period. Trends significant at the 99% and 90% confidence levels are marked by larger filled and hollow triangles, respectively. Smaller triangles indicate trends that are not significant at the 90% level (Zhang et al., 2001).

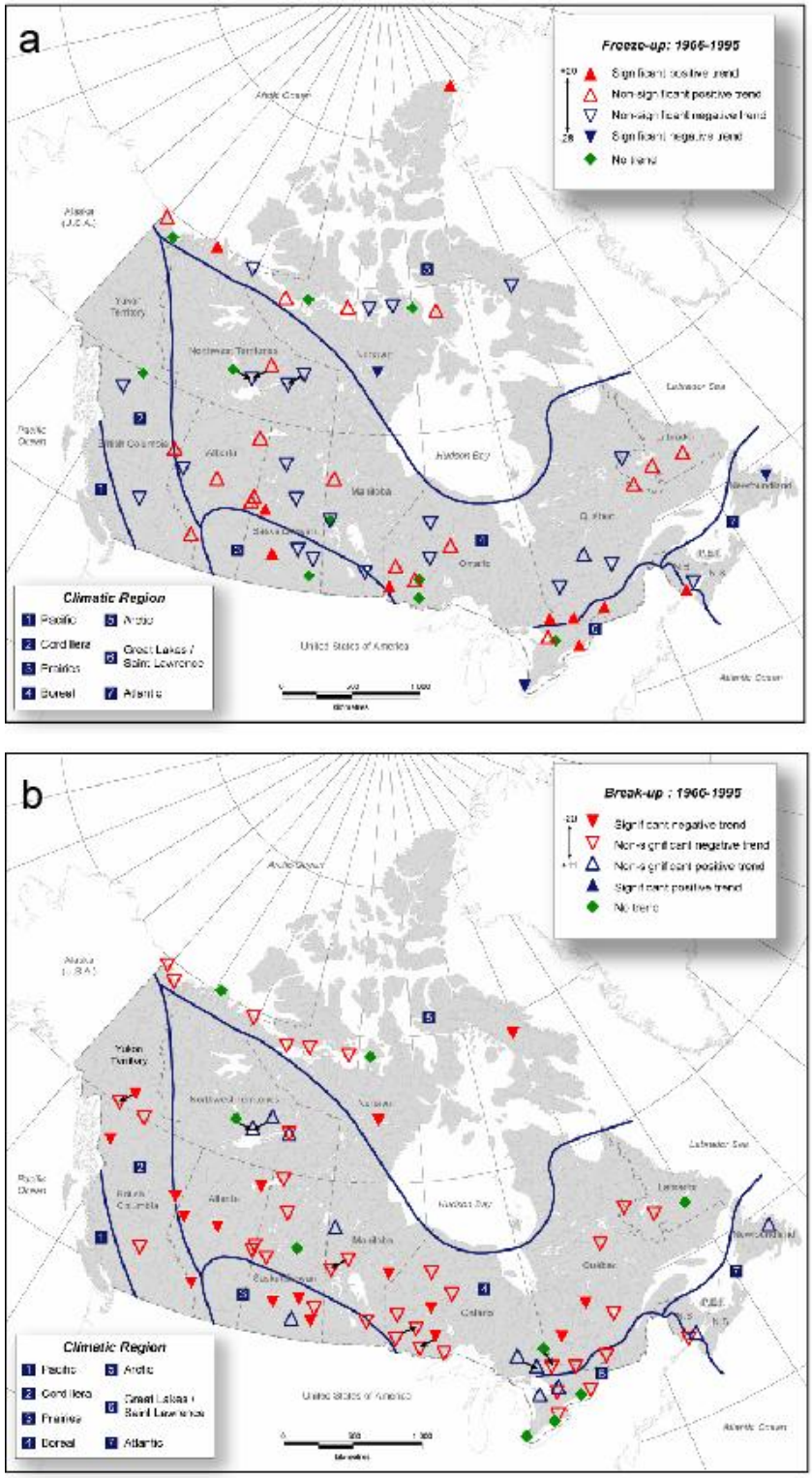

Figure 4.7. Trends in (a) freeze-up and (b) break-up dates observed at lakes in Canada over the period 1965–1995. Downward pointing arrows indicate a trend towards earlier dates; upward pointing arrows, a trend towards later dates. Open symbols indicate that the trend is not significant while solid symbols indicate that the trend is significant at the 90% confidence level. (Modified from Duguay et al., 2006).

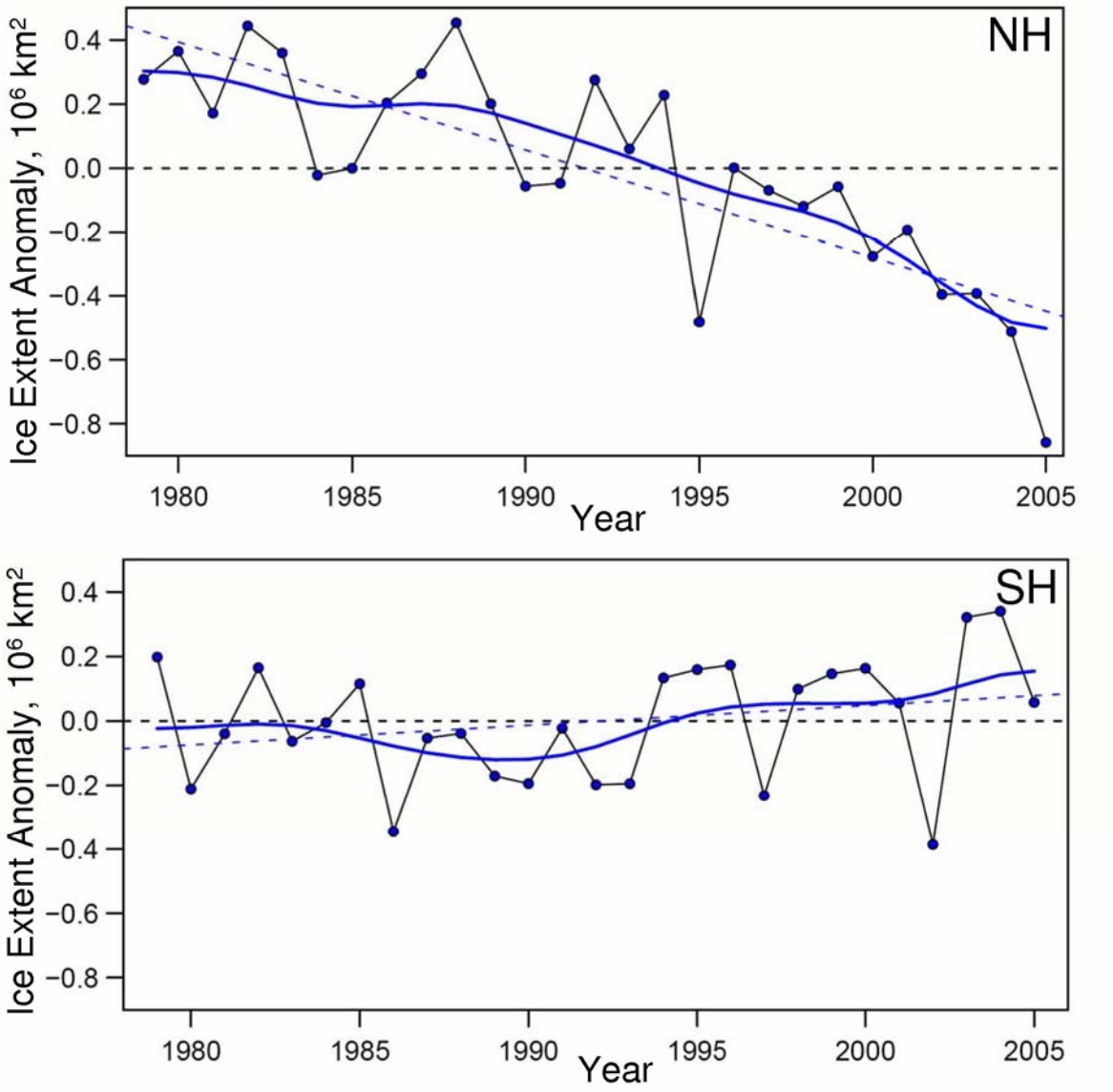

Figure 4.8. Sea Ice extent anomalies for (a) Northern Hemisphere and (b) the Southern Hemisphere based on passive microwave satellite data. Symbols indicate annual mean values while the curve is the result of a 13-point time filter. Linear trend lines are indicated for each hemisphere. For the Arctic, the trend is –33 ± 7.4 x 10^3 km^2 per year (equivalent to approximately -2.7% per decade), whereas the Antarctic results show a small positive trend of 5.6 ± 9.2 x 10^3 km^2 per year. The negative trend in the Northern Hemisphere is significant at the 90% confidence level whereas the small positive trend in the Southern Hemisphere is not significant. (Updated from Comiso, 2003).

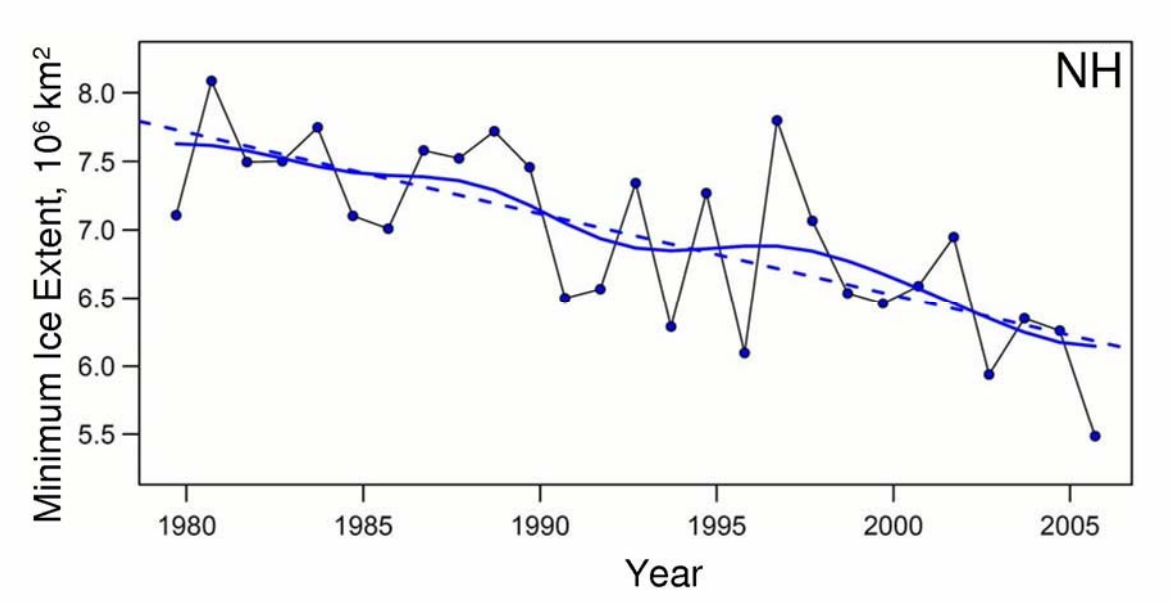

Figure 4.9. Summer minimum Arctic sea ice extent from 1979 to 2005. Symbols indicate annual mean values while the curve is the result of a 13-point time filter. The dashed line indicates the linear trend which is $-60 \pm 20 \times 10^3$ km^2 per year, or approximately –7.4% per decade (updated from Comiso, 2002).

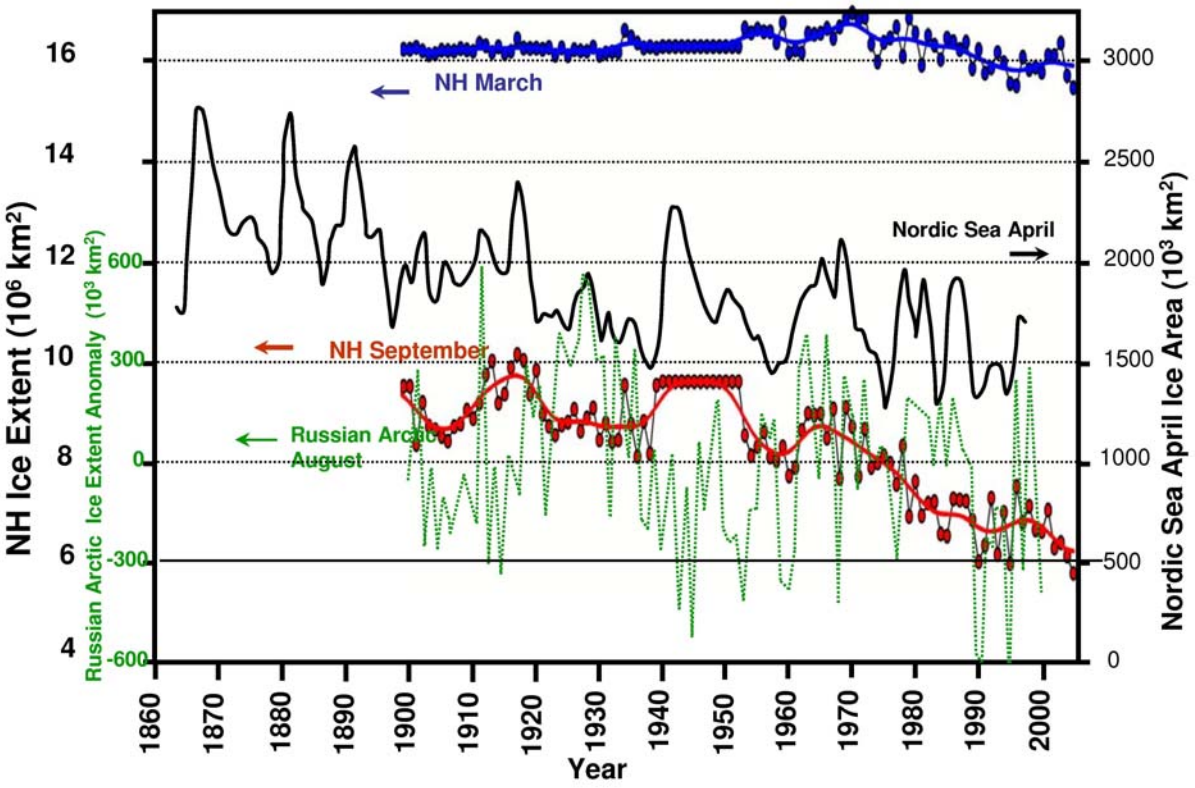

Figure 4.10. Time series of Northern Hemisphere sea ice extent for March and September from the HadISST data set (the blue and red curves, updated from Rayner et al., 2003), the April Nordic Sea ice extent (the black curve, redrafted from Vinje, 2001), and the August ice extent anomaly in the Russian Arctic seas -- Kara, Laptev, East Siberian and Chukchi -- the dotted green curve, redrafted from Polyakov et al., (2003). For the Northern Hemisphere time series, the symbols indicate yearly anomalies while the curve is the result of a 13-point time filter.

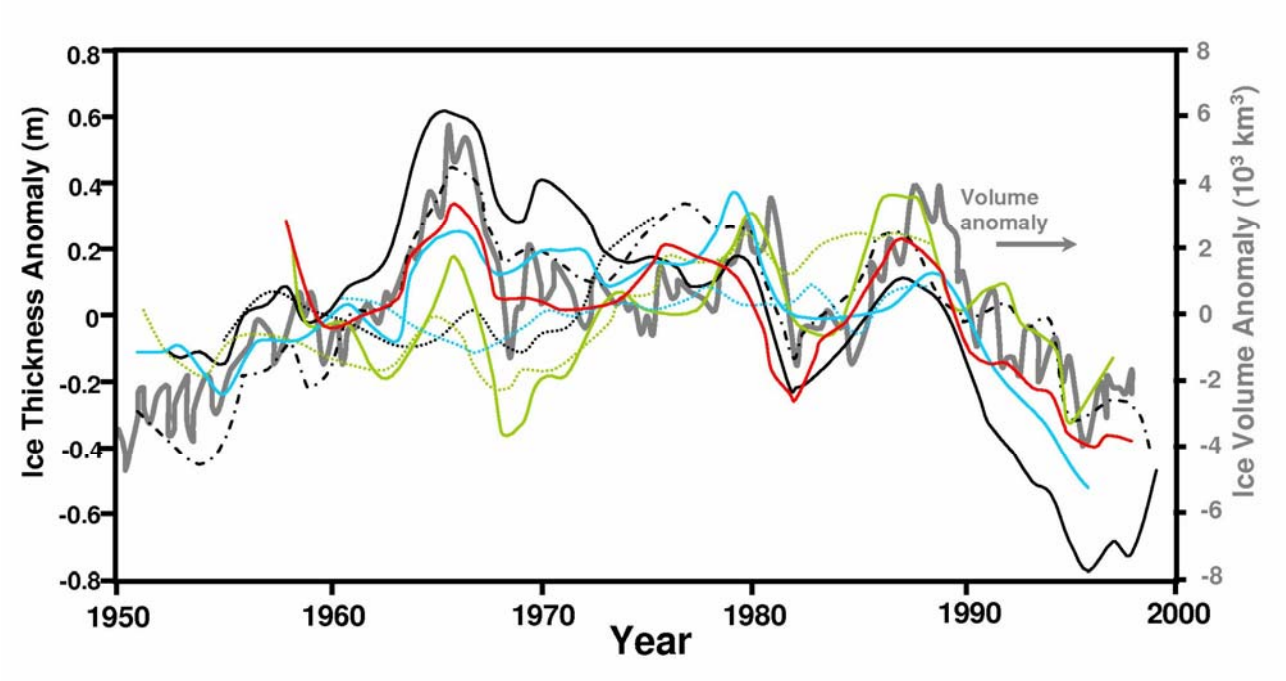

Figure 4.11. Comparison of model-based time series of annual mean, Arctic-basin average sea ice thickness anomaly), obtained from a variety of models (redrafted from Rothrock et al., 2003 – see this paper for identification of the individual models and their attributes), along with the Arctic basin sea ice volume anomalies (grey curve and right-hand scale) computed by Koeberle and Gerdes (2003).

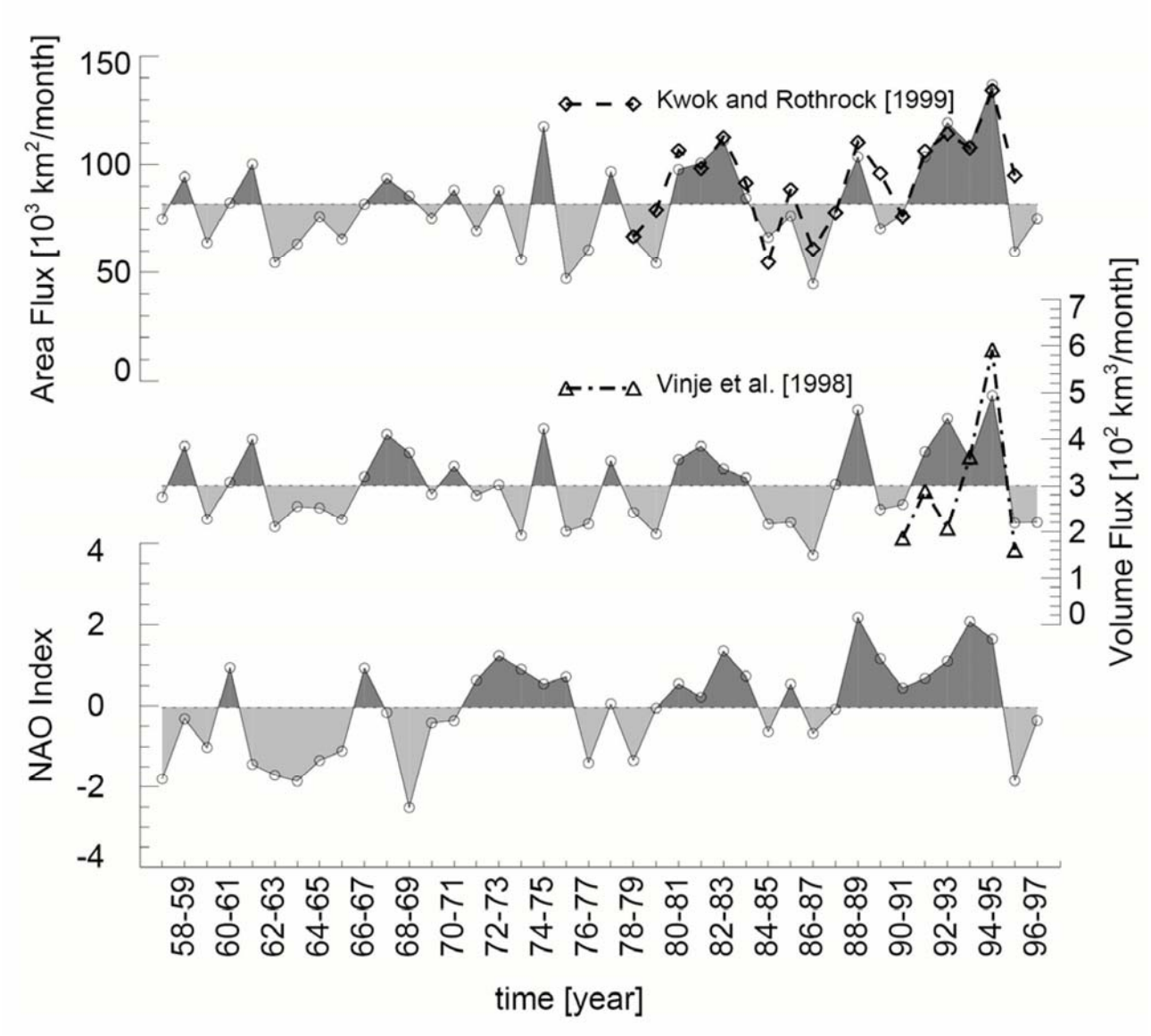

Figure 4.12. Time series of modelled Fram Strait sea ice area and volume flux, along with NAO index. Also shown are observational estimates of area flux (Kwok and Rothrock, 1999) and volume flux (Vinje et al., 1998). This figure is reproduced from Hilmer and Jung (2000).

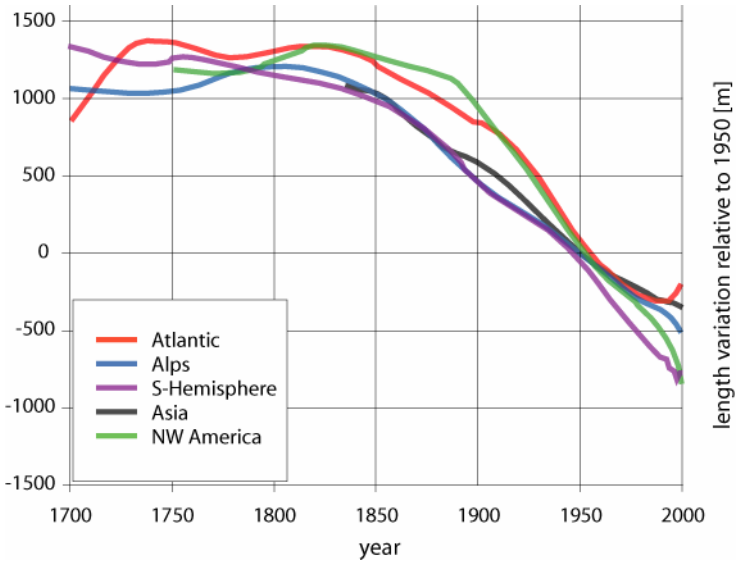

Figure 4.13. Large scale regional mean length variations of glacier tongues (Oerlemans, 2005). The raw data are all constrained to pass through zero at 1950. The curves shown are smoothed with the Stineman method (Stineman, 1980) and approximate this. Glaciers are grouped into the following regional classes: Southern Hemisphere (Tropics, New Zealand, Patagonia), North-West America: (mainly Canadian Rockies), Atlantic (South Greenland, Iceland, Jan Mayen, Svalbard, Scandinavia), (European) Alps; and Asia (Caucasus and Central Asia).

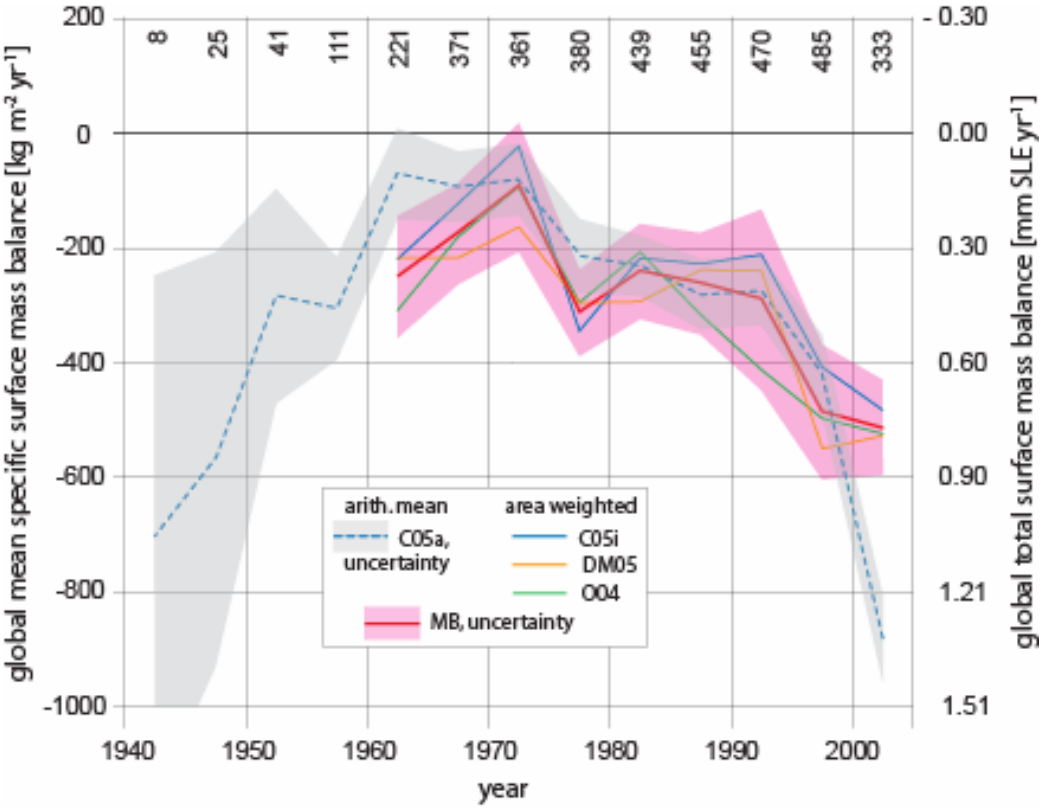

Figure 4.14. Pentadal (five year) average mass balance of the world's glaciers and ice caps excluding those around the ice sheets of Greenland and Antarctica. Mean specific mass balance (left axis) is converted to total mass balance and to sea-level equivalent (right axis) using the respective total ice surface area of 546 x 10^3 km^2 (Table 4.5.1) and the ocean surface area of 362 x 10^6 km^2. C05a is an arithmetic mean over all annual measurements within each pentade (Cogley, 2005); the grey envelope is the 90% confidence level of the C05a data, and represents the spatial variability of the measured mass balances. The number of measurements is given at the top of the graph. C05i is obtained by spatial interpolation (Cogley, 2005), while DM05 (Dyurgerov and Meier, 2005) and O04 (Ohmura, 2004) are area-weighted global numbers. MB is the arithmetic mean of C05i, DM05 and O04. Its uncertainty (red shading) combines the spatial variability and the structural uncertainty (Chapter 3, Section 3.4.1.5). It is calculated for the 90% confidence level. This does not include uncertainties that derive from uncertainties in the glacier area inventories. The authors made area weighting and spatial interpolation only after 1960, when up to 100 measured mass balances were available. The most recent time period consist of four years only (2000/2001–2003/2004).

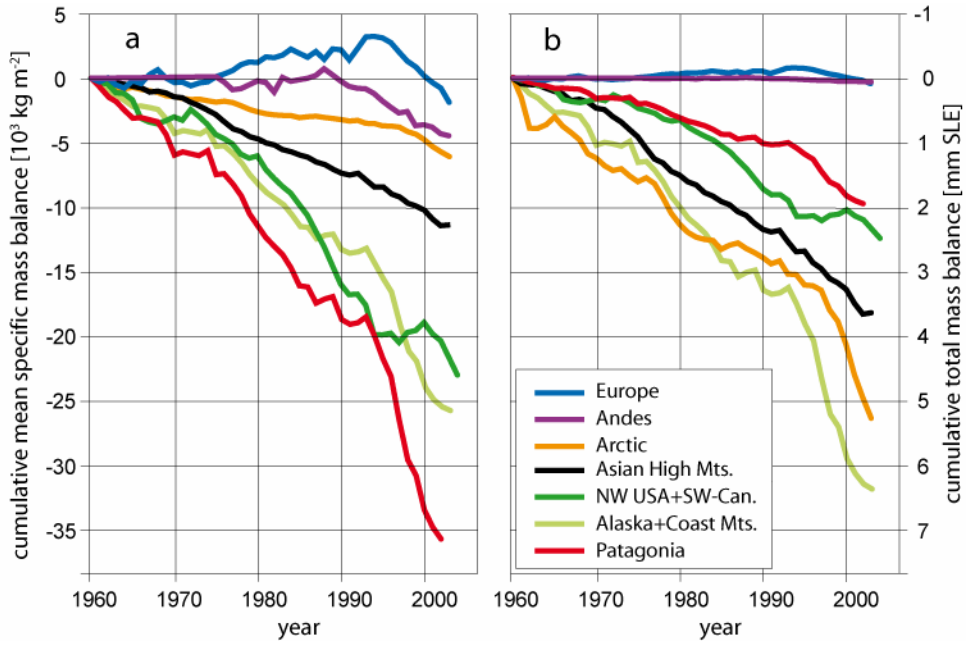

Figure 4.15. Cumulative mean specific mass balances (a) and cumulative total mass balances (b) of glaciers and ice caps, calculated for large regions (Dyurgerov and Meier, 2005). Mean specific mass balance shows the strength of climate change in the respective region. Total mass balance is the contribution from each region to sea-level rise.

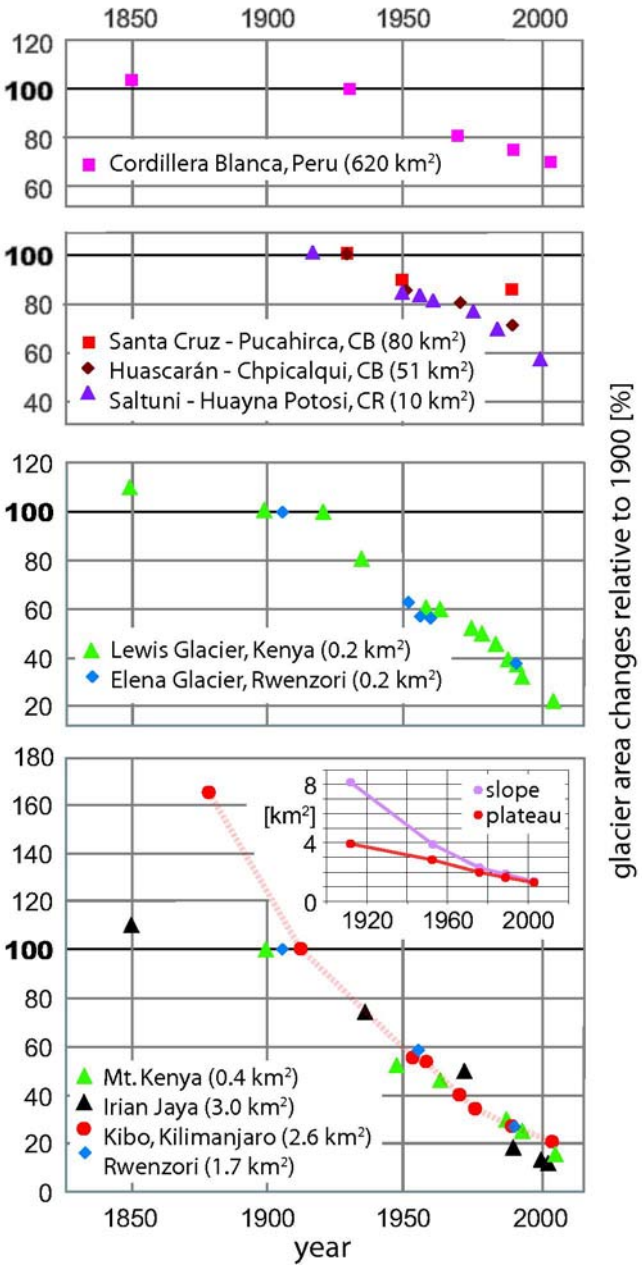

Figure 4.16. Changes in surface area of tropical glaciers relative to their extent around 1900, grouped according to different glacier sizes. The sizes are given for 1990 or the date closest to 1990 available. The broken red line highlights the retreat of Kilimanjaro glaciers. The insert shows the area change (in km^2) of Kilimanjaro plateau (red) and slope (purple) glaciers as separated by the 5700 m contour line. (Cullen et al., 2006; Georges, 2004; Hastenrath, 2005; Kaser and Osmaston, 2002 (updated courtesy of S. Lieb); Klein and Kincaid, 2006; Mölg et al., 2003b).

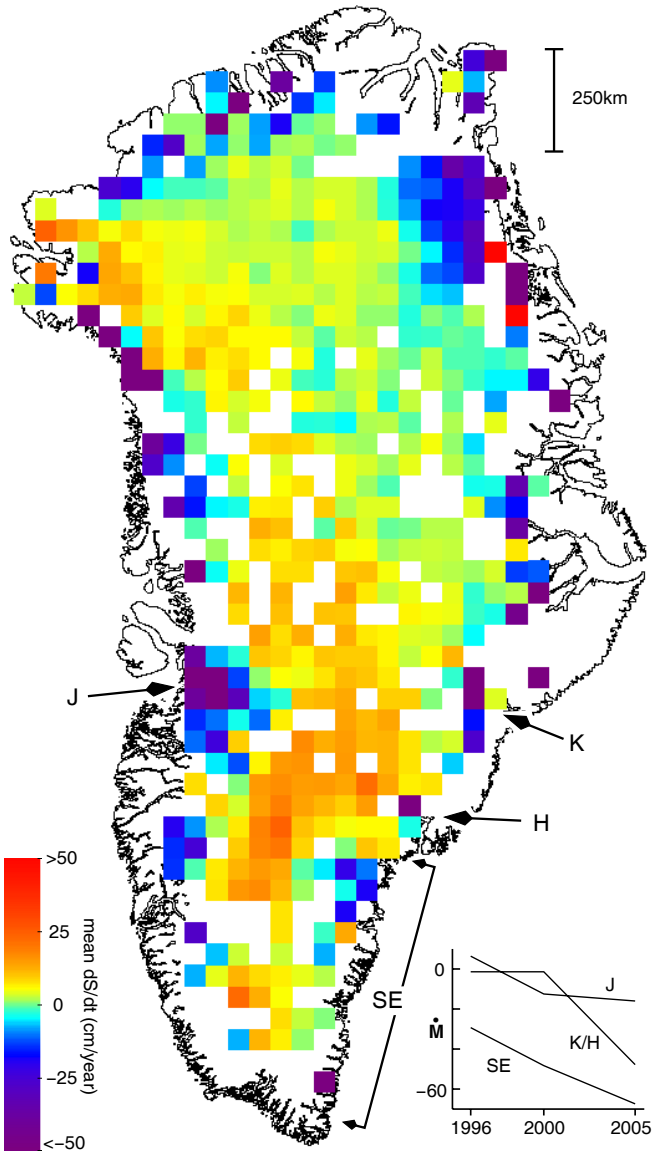

Figure 4.17. Rates of elevation change (dS/dt) derived from laser-altimeter measurements at more than 16,000 locations on the Greenland Ice Sheet where ICESat data from 2005 overlay aircraft surveys in 1998/1999 (using methods described by Thomas et al., 2006). Locations of rapidly-thinning outlet glaciers at Jakobshavn (J), Kangerdlugssuaq (K), Helheim (H) and along the southeast coast (SE) are shown, together with an inset showing their estimated total mass balance ($\dot{\mathbf{M}}$, Gt/yr) between 1996 and 2005 (Rignot and Kanagaratnam, 2006).

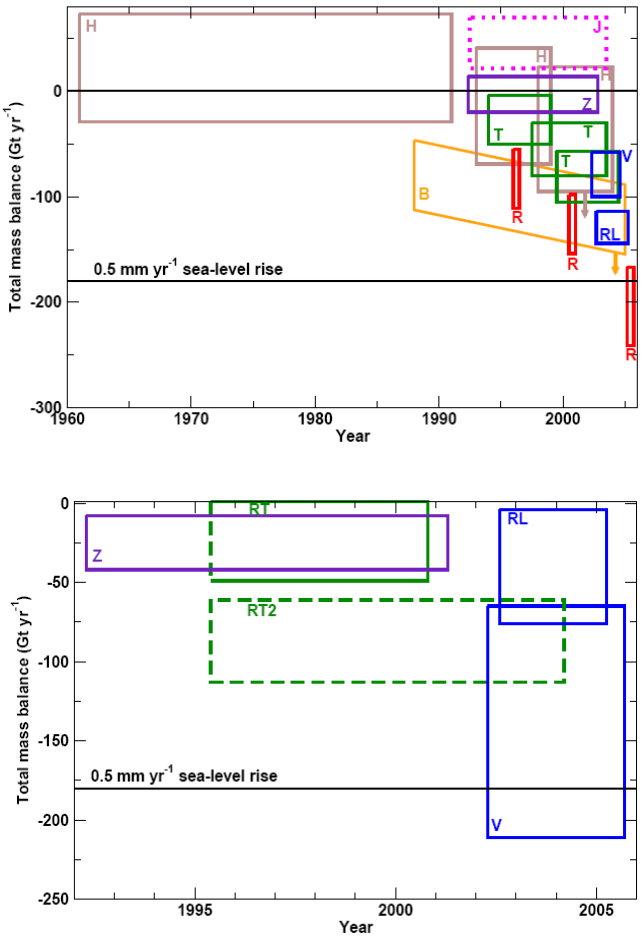

Figure 4.18. Top) Mass-balance estimates for Greenland. The colored rectangles, following Thomas et al. (2006), indicate the age span over which the measurements apply, and the estimate range, given as (mean+uncertainty) and (mean-uncertainty) as reported in the original papers. Code: B (orange; Box et al, 2006), surface mass balance, using stated trend in accumulation, assumed-constant ice-flow discharge, and standard error on regression of accumulation trend, with added arrow indicating additional loss from ice-flow acceleration; H (brown; Hanna et al., 2005), surface mass balance, with arrow as for B; T (dark green; Thomas et al., 2006), laser altimetry, showing new results and revision of Krabill et al. (2004) to include firn-densification changes; Z (violet; Zwally et al., 2006), primarily radar altimetry, with uncertainty reflecting the difference between a thickness change due to ice everywhere and that due to low-density firn in the accumulation zone; R (red; Rignot and Kanagaratnam, 2006), ice discharge combined with surface mass balance; V (blue; Velicogna and Wahr, 2005) GRACE gravity; RL (blue; Ramillen et al., 2006) GRACE gravity; J (magneta dashed; Johannessen et al., 2005), radar altimetry without firn-densification correction and applying only to central regions that are thickening but omitting thinning of coastal regions. Bottom) Mass-balance estimates for grounded ice of Antarctica. Colored rectangles show age span and error range as in the top panel. Code: Z (violet; Zwally et al., 2006), radar altimetry, with uncertainty reflecting the difference between a thickness change due to ice everywhere and that due to low-density firn everywhere; RT (dark green; Rignot and Thomas, 2002), ice discharge and surface mass balance, with dashed end line because some of the accumulation-rate data extend beyond the time limits shown; RT2 (dark green; Rignot and Thomas, 2002), updated to include additional mass losses indicated by Thomas et al. (2004) and Rignot et al. (2005), dashed because the original authors did not produce this as a whole-ice-sheet estimate nor are accumulation rates updated; V (blue; Velicogna and Wahr, 2006), GRACE gravity; RL (blue; Ramillen et al., 2006) GRACE gravity.

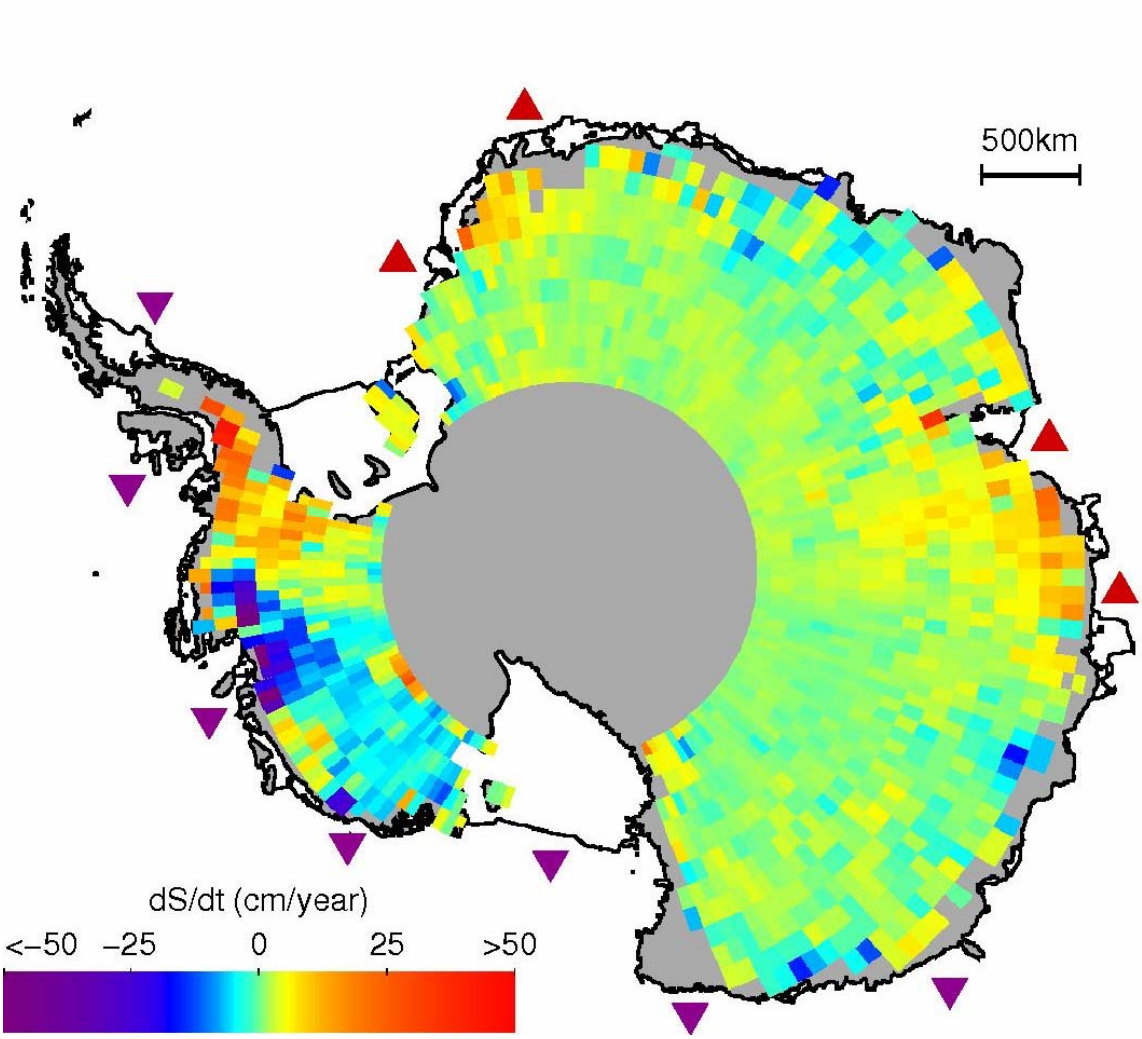

Figure 4.19. Rates of elevation change (dS/dt) derived from ERS radar-altimeter measurements between 1992 and 2003 over the Antarctic Ice Sheet (Davis et al., 2005). Locations of ice shelves estimated to be thickening or thinning by more than 30 cm a^{-1} (Zwally et al., 2006) are shown by red triangles (thickening) and purple triangles (thinning).

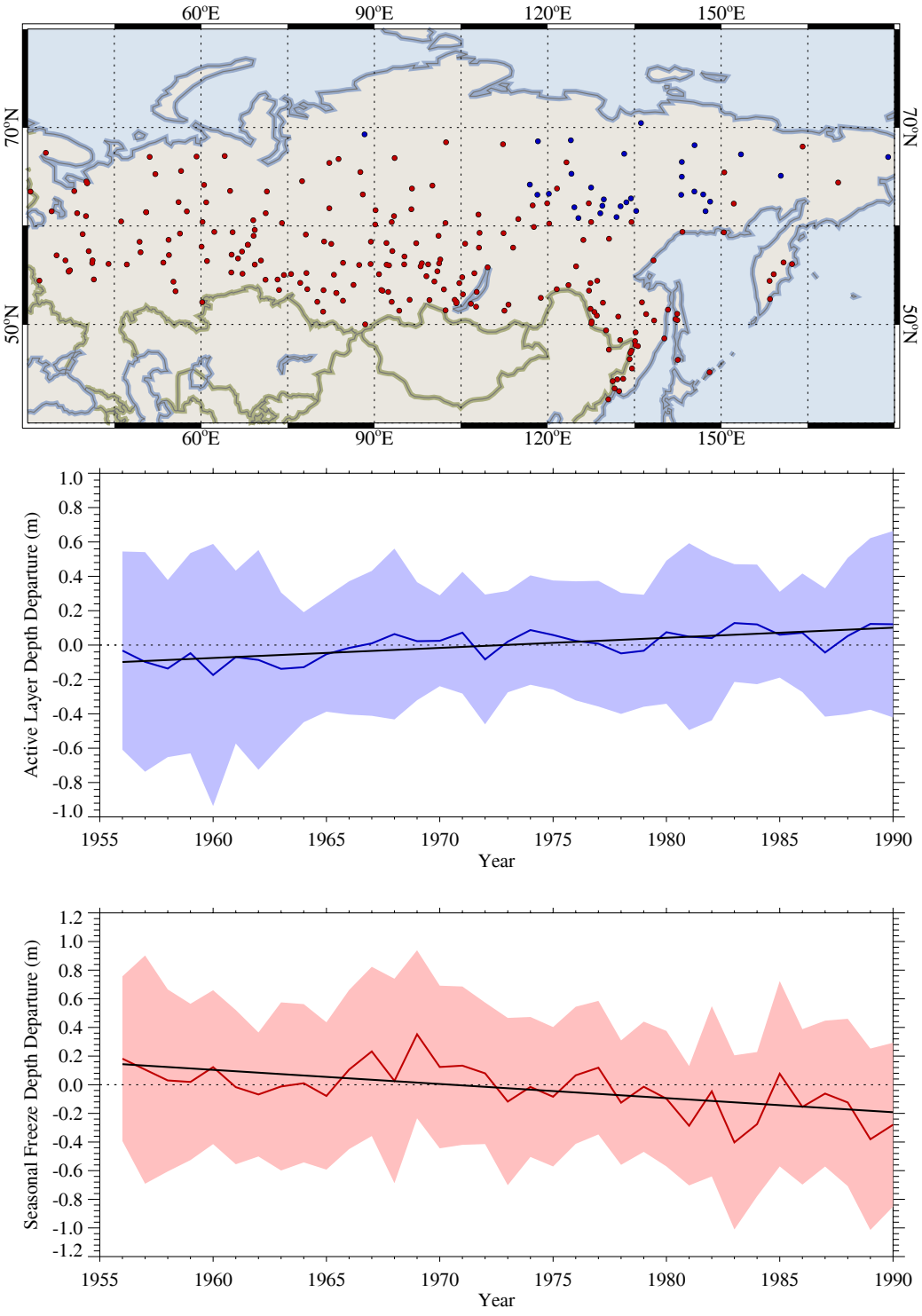

Figure 4.20. Variations of the thickness of the active layer over permafrost (middle) and maximum soil freeze depth in non-permafrost area (lower) in Russia from 1956 through 1990. Active layer thickness has increased by about 20 cm while seasonal freeze depth has decreased by about 34 cm over the period of record (black lines in middle and lower panels). Anomaly of active layer thickness (thin blue line) is an average of anomalies from 31 stations (blue dots on the top panel) after removing the mean over the period of record for each station. Anomaly of maximum soil freeze depth is an average of anomalies from 211 stations (red dots on the top panel) after removing the mean over the period of record for each station. The shaded area represents the 5–95% confidence interval from the mean for each year; the dashed-line is the zero reference (from Frauenfeld et al., 2004).

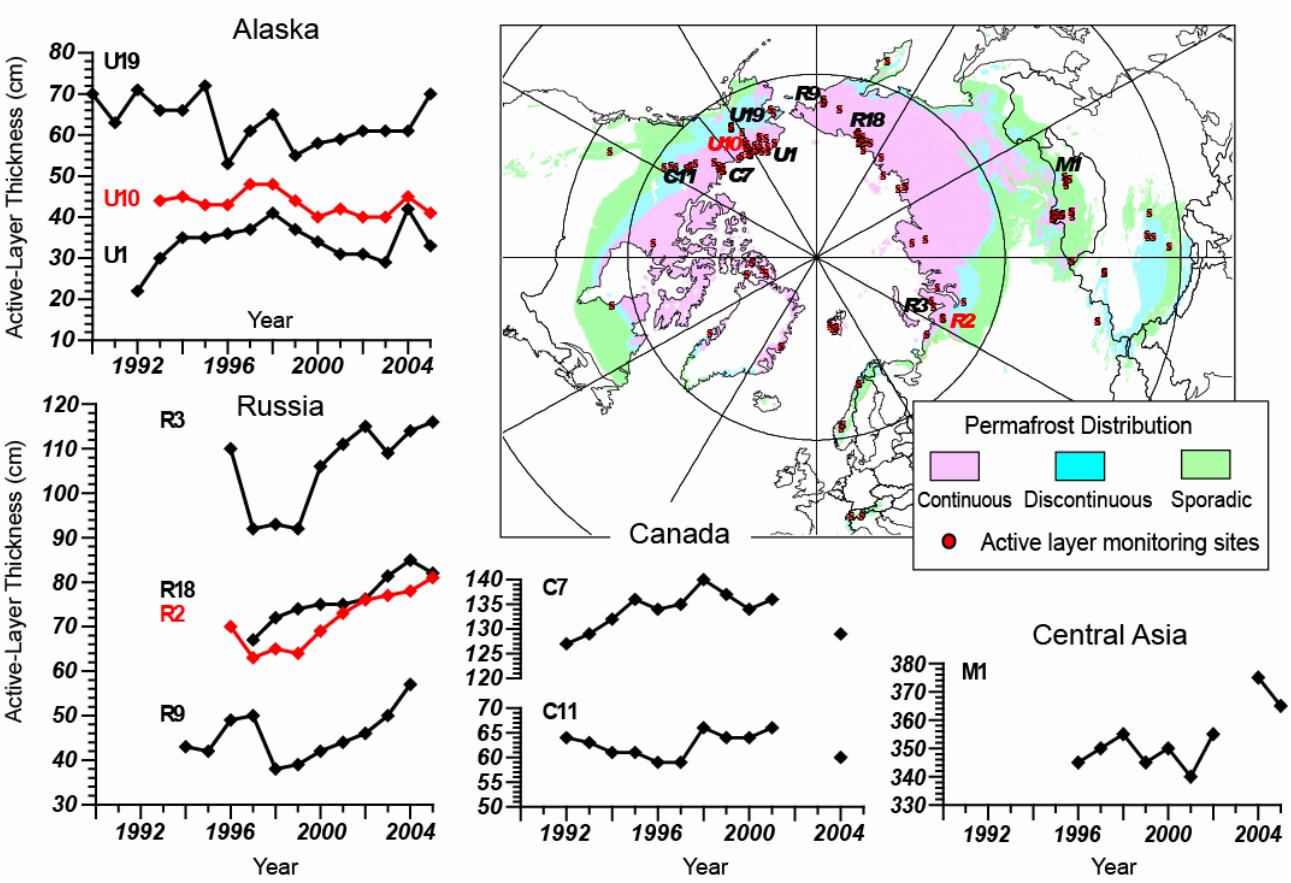

Figure 4.21. Locations of sites and changes in active layer thickness (ALT) from selected sites (after Nelson, 2004).

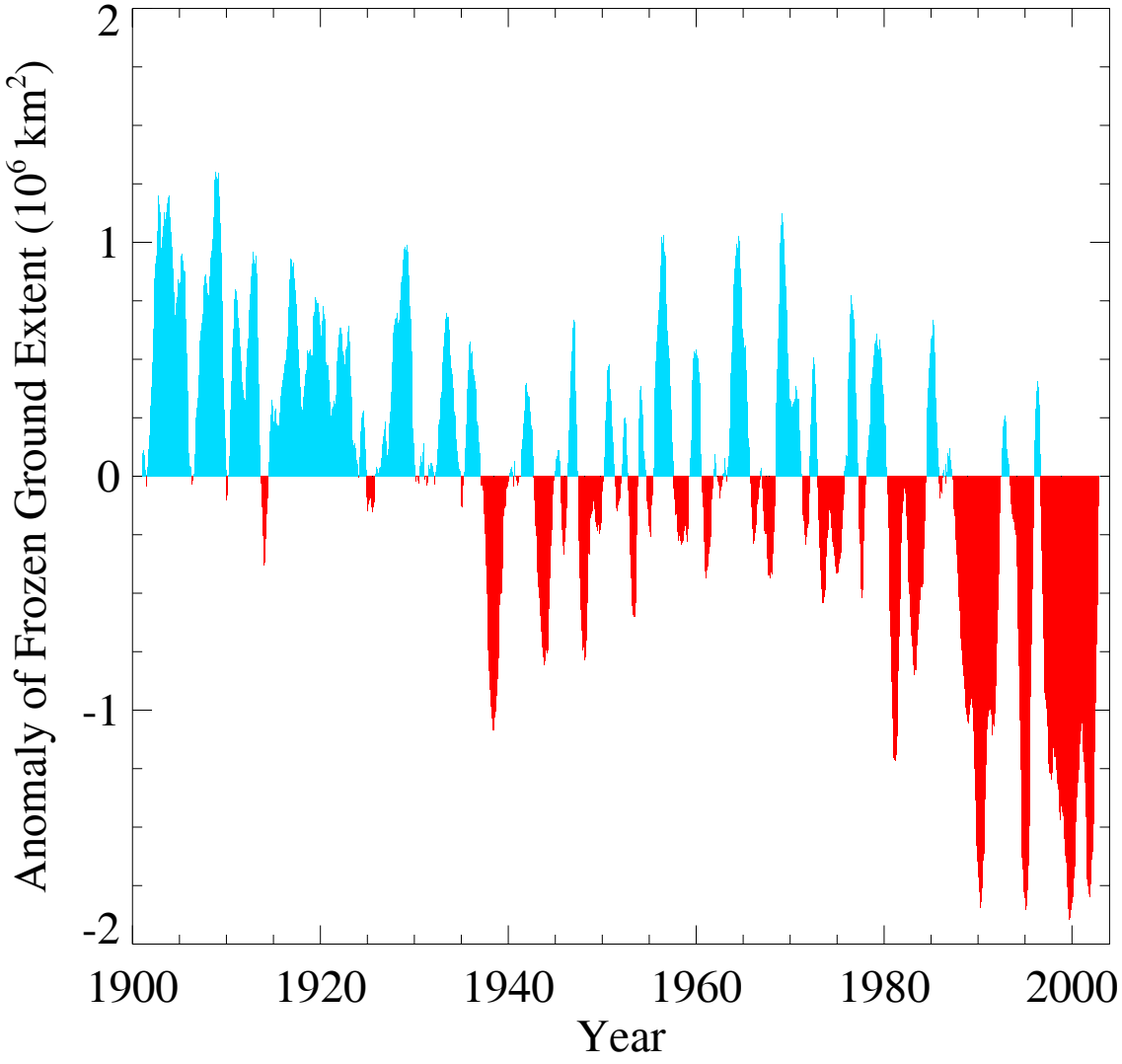

Figure 4.22. Historical variations of the monthly extent of the area of seasonally frozen ground (including the active layer over permafrost) for the period from 1901 through 2002 in the Northern Hemisphere. The positive anomaly (blue) represents above monthly average extent, while negative anomaly (red) represents below average extent. The time series is smoothed with a low-pass filter. (After Zhang et al., 2003).

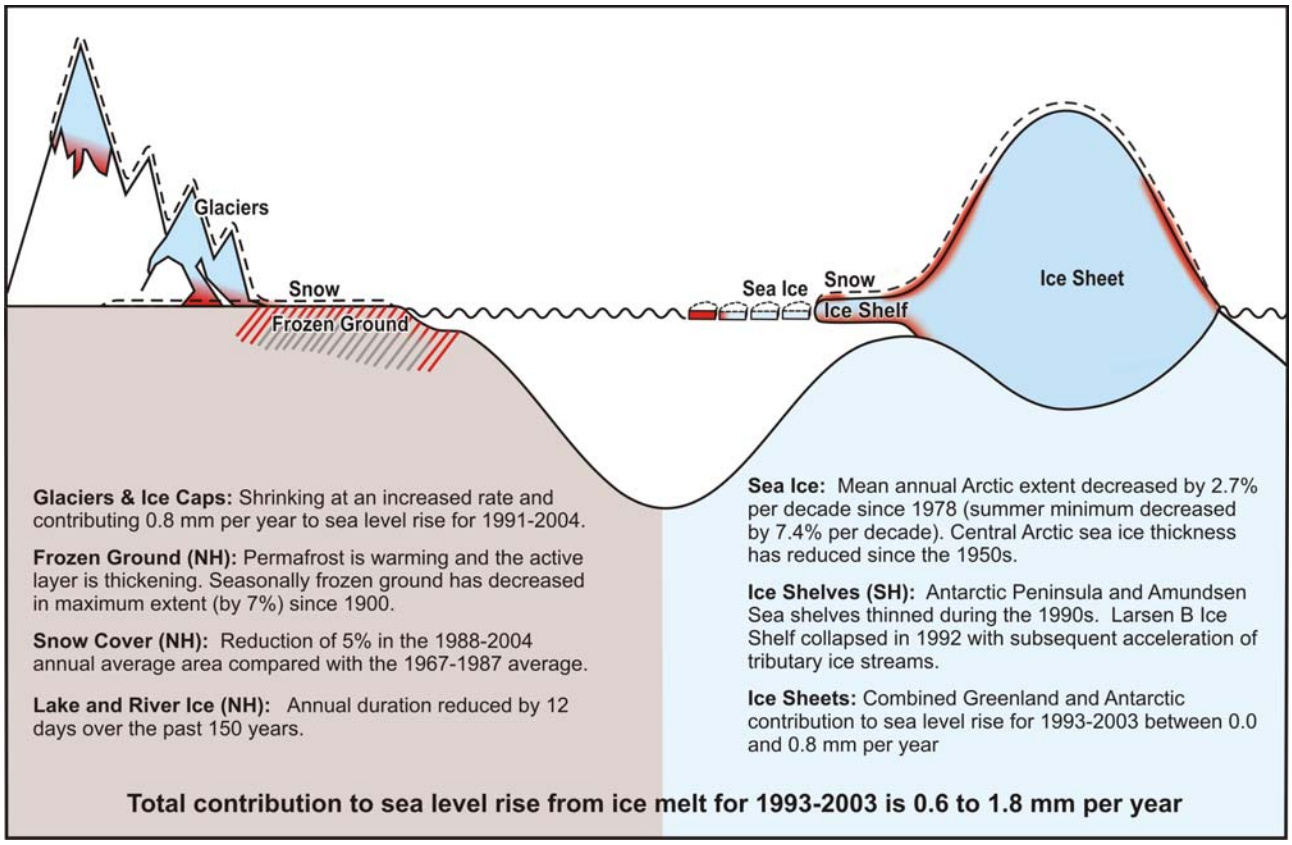

Figure 4.23. Summary of observed variations of the cryosphere.

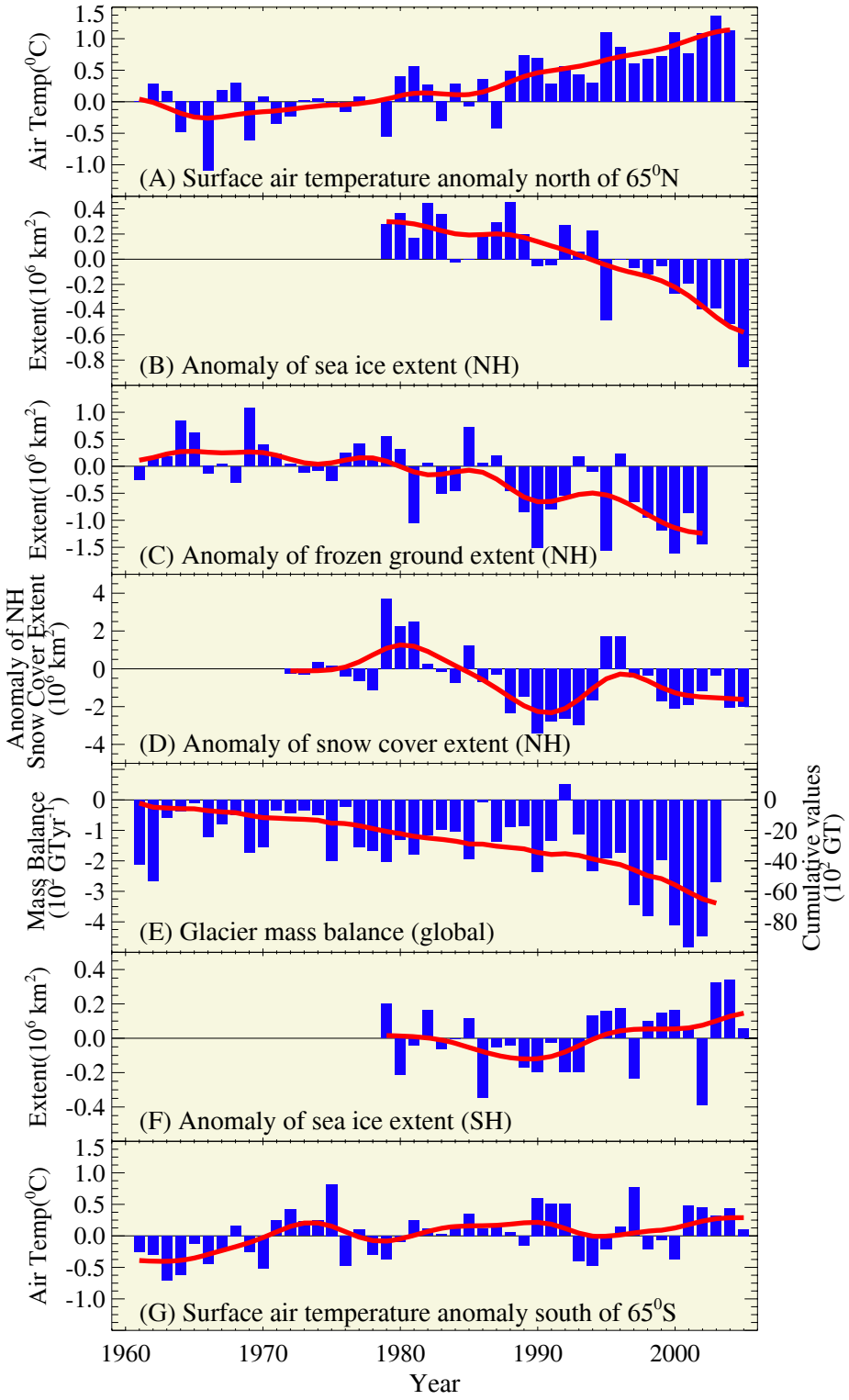

FAQ 4.1, Figure 1. Anomaly time series (departure from the long-term mean) of polar surface air temperature (A, G), Arctic and Antarctic sea ice extent (B, F), Northern Hemisphere (NH) frozen ground extent (C), NH snow cover extent (D) and global glacier mass balance (E). The solid red line in E denotes the cumulative global glacier mass balance; otherwise it represents the smoothed time series using a 13-point filter (see Chapter 3).